Characteristics of distinct thermal transport behaviors in single-layer and multilayer graphene

Cuiqian Yu, Shuyue Shan, Shuang Lu, Zhongwei Zhang,* and Jie Chen†

Center for Phononics and Thermal Energy Science, China–EU Joint Lab for Nanophononics, MOE Key Laboratory of Advanced Micro-structured Materials, School of Physics Science and Engineering, Tongji University, Shanghai 200092, People's Republic of China

(Received 25 December 2022; revised 31 March 2023; accepted 17 April 2023; published 27 April 2023)

As a crucial signature of hydrodynamic phonon transport, second sound is currently raising research attention in the field of non-Fourier heat conduction. In this work, through molecular dynamics simulations, the fundamental characteristics of second sound are explored from a transient heat conduction modeling in the single-layer and multilayer graphene and graphite. Our simulation results demonstrate that second sound can carry more heat energy and maintain for a longer lifetime than that of the ballistic pulse. The underlying mechanisms are carefully discussed from the modal energy analysis. In addition, we also unveil that the thickness in multilayer graphene and graphite significantly suppresses the propagation of second sound due to the enhanced weight of umklapp scattering. The effects of excitation temperature and ambient temperature on the second sound are also studied. Our simulation results reveal that the second sound in single-layer graphene can persist up to 110 K. This work provides valuable insight into the basic characteristics of second sound, which should be critical in the understanding of hydrodynamic phonon transport and thermal physics in graphene and its derivatives.

DOI: 10.1103/PhysRevB.107.165424

I. INTRODUCTION

Hydrodynamic phonon transport [1–3] is one of the unique thermal transport behaviors beyond the well-established ballistic and diffusive transport pictures [4–6]. In the hydrodynamic regime, phonons propagate in the form of collective phonon drift motion due to the dominance of the momentum-conserving normal (N) process in the phonon-phonon scattering processes [1–3,7–10]. Hydrodynamic phonon transport is associated with diverse thermal transport phenomena, such as the second sound [7,11–15], Poiseuille flow [8,11,16], and phonon Knudsen minimum [17,18]. Second sound is a crucial signature of phonon hydrodynamics, in which heat propagates in a wavelike form, exhibiting the non-Fourier heat conduction behavior [9,12,19].

Previously, second sound has been merely observed in three-dimensional systems at ultralow temperatures [20–26], such as in superfluid ^{3}He at 0.42–0.58 K [23], in Bi at 1.2–4.0 K [24], and in NaF at 11–14.5 K [25,26]. Because the unique flexural acoustic (ZA) modes in two-dimensional (2D) systems could result in the pronounced N process, recent advances [8,10] showed that more intriguing performances of phonon hydrodynamics, including second sound and Poiseuille flow, emerged in 2D materials and their derivatives, in which graphene and graphite are the most ideal platforms [27–29]. For instance, Huberman *et al.* [10] experimentally observed second sound in graphite thin film above 100 K through a time-resolved optical measurement. Ding *et al.* [19] further reported that the temperature window of second sound in graphite can reach as high as 200 K. However, the fundamental characteristics of second sound remain elusive in these experimental studies. In addition, Machida *et al.* [30] experimentally found that the thickness has a significant effect on hydrodynamic phonon transport and thermal conductivity of graphite thin film, in which the ZA phonons are believed to be responsible. However, the fundamental relation between ZA phonons and the characteristics of phonon hydrodynamics (e.g., second sound) requires further investigation, especially for the thickness effect.

Based on the phonon Boltzmann transport equation (BTE), second sound has been widely investigated from various relevant parameters [2,7–9,13–15], including the drifting component [2,9], propagation length [9], propagation speed [7,8,13], and temperature window [8]. On the other hand, classical molecular dynamics (MD) simulation is capable of modeling the transient propagation process of second sound via the real-space physical quantities [31–34], although it fails in considering the quantum effect. For instance, Yao and Cao [34] studied the propagation of ballistic and second sound pulses in the single-layer graphene ribbons based on MD simulations. However, the speed of second sound reported in their work is quite different from other studies [3,7,8,13]. Besides, they found that second sound is dominated by the transverse acoustic (TA) phonons [34], contrary to the widely accepted role of ZA phonons [3,35]. These contradictions between literature studies make the physics of second sound remain elusive. Moreover, the propagation of heat energy in the form of second sound is still puzzling, especially at a modal level of understanding, in contrast to the well-known ballistic and diffusive transport.

In this work, we characterize the properties of second sound in single-layer and multilayer graphene and graphite from a transient heat conduction modelling through MD

*Corresponding author: zhongwei@tongji.edu.cn
†Corresponding author: jie@tongji.edu.cn

simulations. The propagations of ballistic pulse, second sound, and diffusive phonons are systematically studied in terms of modal analysis and decaying characteristics. Then, we investigate the dependence of second sound on the thickness in multilayer graphene, which is further explained by the variation of ZA phonons and weight of umklapp (U) scattering. Finally, the impacts of excitation temperature and ambient temperature on the second sound are also investigated. This work provides fundamental understandings on the physics for the second sound phenomenon in graphene systems and its derivatives.

The rest of this paper is organized as following: Section II describes the details of MD simulations and the calculations of phonon modal energy. Then, we discuss the main results in Sec. III. The modal analysis and decay processes of ballistic pulse, second sound, and diffusive phonons are studied in Secs. III A and III B, respectively. The dependence of second sound on the thickness is discussed in Sec. III C. The effects of the excitation temperature and the ambient temperature are presented in Sec. III D. Finally, we conclude this work in Sec. IV.

II. METHODS

A. MD simulations

All MD simulations are performed with the LAMMPS package [36]. Compared to previous BTE studies [2,8], MD simulations can more intuitively simulate the dynamic propagation process of phonons. Graphene based systems are ideal platforms to explore hydrodynamic phonon transport because of the intrinsically pronounced N phonon-phonon scattering from ZA phonons [37–39]. The simulation systems considered in this work include single-layer and multilayer graphene and graphite. The intralayer atomic interaction between C-C bonds in these graphene systems is described by the optimized Tersoff potential [40]. In addition, the interlayer van der Waals interaction is described by Lennard-Jones potential $V(r_{ij}) = 4\varepsilon[(\sigma_{ij}/r_{ij})^{12} - (\sigma_{ij}/r_{ij})^{6}]$ with the optimized parameters taken from Ref. [41]. These empirical potentials have been shown to reliably describe the thermal transport properties of graphene and its derivatives [4,38,42–45]. Moreover, previous studies [14,46] have shown that the high-frequency optical branches have a negligible contribution in phonon hydrodynamics, as the second sound only appears at low temperatures and is dominated by low-frequency phonons. Therefore, the accurate description of acoustic phonons by these empirical potentials can provide reliable simulations of the second sound. The periodic boundary conditions are applied to all directions, and the time step is set as 0.5 fs. To eliminate the artificial cross-boundary interaction along the vertical direction, a vacuum layer of 20 Å in thickness is added to the out-of-plane direction in the simulation domains of single-layer and multilayer graphene.

Figure 1(a) shows the simulation setup for the transient heat conduction process in single-layer graphene. To clearly simulate the propagation of heat pulse in a large spatial and temporal scale, we set the sample length to 1 μm, which is sufficient to obtain the length-independent temperature distribution in single-layer graphene (see Fig. S1 of the

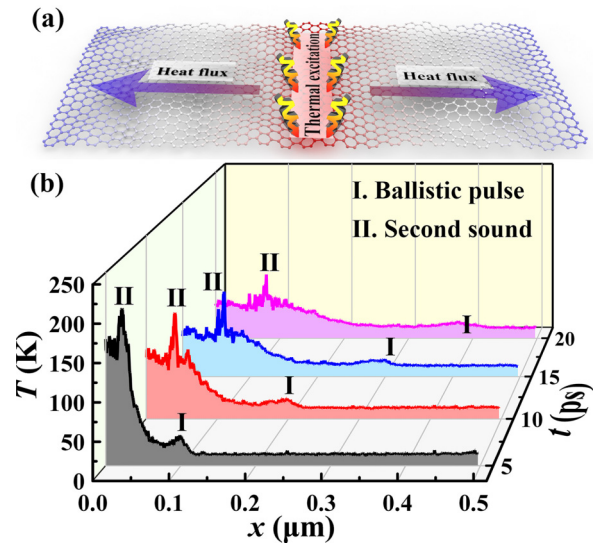

FIG. 1. (a) The simulation setup of transient heat conduction process in single-layer graphene. A high-temperature thermal excitation is applied to the central region, leading to the heat flux propagation towards two sides. The length direction is along the heat flux, while the width direction is perpendicular to the heat flux. (b) Temperature distribution of single-layer graphene along the length direction at 5, 10, 15, 20 ps. Here, the length is 1 μm, $T_{amb} = 20$ K and $T_{exc} = 4000$ K. The symbols I and II in (b) denote the ballistic pulse and second sound, respectively.

Supplemental Material [47]). Meanwhile, the width of the samples is 9 nm, which is large enough to suppress the width effect with the use of the periodic boundary condition. For the multilayer graphene and graphite, the interlayer distance is initially set as 0.34 nm. In our MD simulations, we first thermalize the whole system with the canonical ensemble at ambient temperature T_{amb} of 20 K for 250 ps to reach thermal equilibrium. Then, we apply thermal excitation at the central region [see Fig. 1(a)] via the velocity rescaling method [48,49] to increase the local temperature to the excitation temperature T_{exc} of 4000 K within 0.5 ps, and further maintain at T_{exc} for another 0.5 ps. After this instantaneous thermal excitation, all thermostats are withdrawn in order to simulate the transient propagation process of heat pulse in the microcanonical ensemble. Such a procedure has been widely used in previous studies to simulate the transient heat conduction process [31–34]. Finally, we collect the temperature data in each local slab with a thickness of 5 Å along the length direction. The local temperature at transient time t_0 is calculated according to the averaged kinetic energy of atoms in each slab as

$$T(t_0) = \frac{1}{3N_S k_B} \sum_i m_i \mathbf{v_i}(t_0) \cdot \mathbf{v_i}(t_0), \tag{1}$$

where N_S is the number of atoms in the slab, k_B is the Boltzmann constant, and m and $\mathbf{v}$ are the mass and the velocity vector of each atom. Since the transient heat conduction process is symmetric with respect to the central region [see Fig. 1(a)], only the simulation results on one side are discussed in the following part.

B. Phonon modal energy

To understand the underlying physical origin of second sound, we calculate the phonon modal energy for each mode λ at an instantaneous time t_0 according to [50]

$$E_\lambda(t_0) = \dot{Q}^*_\lambda(t_0)\dot{Q}_\lambda(t_0), \tag{2}$$

where λ represents a given phonon mode ($\mathbf{k}$, s), with $\mathbf{k}$ denoting the phonon wave vector and s denoting the branch index. The normal mode amplitude $Q_\lambda(t_0)$ is obtained by the Fourier transform of the atomic displacement, and its time derivative $\dot{Q}_\lambda(t_0)$ is defined as [50]

$$\dot{Q}_\lambda(t_0) = \frac{1}{\sqrt{N_c}} \sum_{l,\,b}^{N_c,\,n} \sqrt{m_b} \exp\left(-i\mathbf{k}\cdot\mathbf{r}_{l,b}\right)\mathbf{e}^*_{b,\lambda}\cdot\dot{\mathbf{u}}_{l,b;t_0}. \tag{3}$$

Here, N_c and n are the total number of the unit cells and the number of atoms in a unit cell, m_b is the mass of the bth basis atom, $\mathbf{r}_{l,b}$ is the equilibrium position of the bth basis atom in the lth unit cell, $\mathbf{e}^*_{b,\lambda}$ denotes the complex conjugate of the phonon eigenvector component at the bth basis atom for the mode λ, and $\dot{\mathbf{u}}_{l,b,t_0}$ is the velocity vector of the bth basis atom in the lth unit cell at a given time t_0. The eigenvector $\mathbf{e}_{b,\lambda}$ and eigenfrequency ω can be obtained in the calculation of phonon dispersion by GULP [51]. For each phonon mode ($\mathbf{k}$, s), we compute its modal energy according to Eqs. (2) and (3), and then project this modal energy onto the phonon dispersion relation. This modal energy method has been widely used to analyze the underlying phonon properties [52–54].

III. RESULTS AND DISCUSSION

A. Modal analysis

The transient temperature distribution in Fig. 1(b) shows that two obvious peaks, marked by I and II, are carrying a large amount of heat energy in the single-layer graphene. Interestingly, these two peaks exhibit a distinct peak area and decay rate over time (see the detailed discussion in Sec. III B). In order to identify the nature of peaks I and II, we first calculate the velocity of these two peaks by tracking their positions versus time.

The propagation speed of peak I calculated from MD simulation is 18.7 km/s. Meanwhile, we calculate the group velocities of TA and longitudinal acoustic (LA) phonons near the Γ point (sound velocities) from the phonon dispersion relation, and obtain the sound velocities as 15.0 and 21.9 km/s for TA and LA phonons, respectively. Our calculation results are consistent with the results (13.6 km/s for TA and 21.3 km/s for LA) reported by Luo *et al.* [7]. Therefore, the propagation speed of peak I (18.7 km/s) falls between the sound velocities of TA and LA phonons, indicating the ballistic nature of the peak I. This conclusion is further supported by the reasonably good agreement between the propagation speed of peak I and the propagation speed of ballistic pulse recorded in literature studies [7,34], as listed in Table I. The small difference might be caused by the different ambient temperature T_{amb} and interaction potentials used in the simulations.

The propagation speed of peak II calculated from MD simulation is 3.8 km/s, which is much slower than that of peak I. In addition, we also analytically calculate the second sound velocity v_{II} in the transport direction (x direction) according to the theory described in Refs. [19,55] as

$$v_{\text{II}} = \sqrt{\frac{\left(\sum \frac{C_k k_x v_x}{\omega_k}\right)^2}{\sum \frac{C_k k_x^2}{\omega_k^2} \sum C_k}}, \tag{4}$$

where C_k, k_x, v_x, and ω_k are the mode heat capacity, wave vector, group velocity, and frequency, respectively. All phonon modes are considered in the summation in Eq. (4). To ensure the consistency with our MD simulation results, we predict the velocity of the second sound from Eq. (4) based on classical statistics ($C_k = k_B$), where all the phonon modes are equally excited [56]. The prediction result from Eq. (4) is 3.7 km/s, which agrees very well with the measured propagation speed of peak II in our MD simulations (3.8 km/s). Such agreement confirms that peak II has the nature of the second sound. Therefore, these two peaks in Fig. 1(b) correspond to the ballistic pulse (peak I) and second sound (peak II), respectively, which is consistent with previous studies [7,31,34].

TABLE I. Propagation speed of the ballistic pulse and second sound in the single-layer graphene. The bracket in the last column indicates the nature of phonon statistics used in the calculation.

T_{amb} (K)	Ballistic pulse (km/s)	Second sound (km/s)	Source
20	18.7	3.8	This work (classical)
25	Not available	2.1	Lee *et al.* [8] (quantum)
30	13.6/21.3	2.0	Luo *et al.* [7] (quantum)
50	Not available	5.0	Shang *et al.* [13] (quantum)
50	14.3	9.3	Yao and Cao [34] (classical)

Table I compares the values of second sound from our study and literature results [7,8,13,34]. The quadratic phonon dispersion of ZA causes the group velocity to be frequency dependent as well as the ambient temperatures [8], which would further result in the temperature-dependent propagation speed of second sound due to the quantum statistics. As a result, the results in Table I reveals that the classical statistics in our MD simulation tends to overestimate the velocity of the second sound, compared to the literature results. More detailed discussions on the temperature effect of the second sound velocity can be found in Sec. III D. In addition, the sample size and simulation time should be sufficient to ensure the occurrence of N scattering, as demonstrated by previous studies [8,10], which might be responsible for the discrepancy between our simulation result and previous MD simulation result [34].

To provide physical insights to the transport behavior behind these two peaks and also the nonpeak region from a modal level, we independently project the phonon modal energy in each local region as shown in Fig. 2(a), where two peaks and a typical nonpeak region emerge, into the full phonon dispersion along the high symmetric path Γ-*M*-*K*-Γ. Here, the total number of the unit cells N_c in these three regions are sufficiently large to ensure the convergence. To track the modal results over the whole heat flux propagation

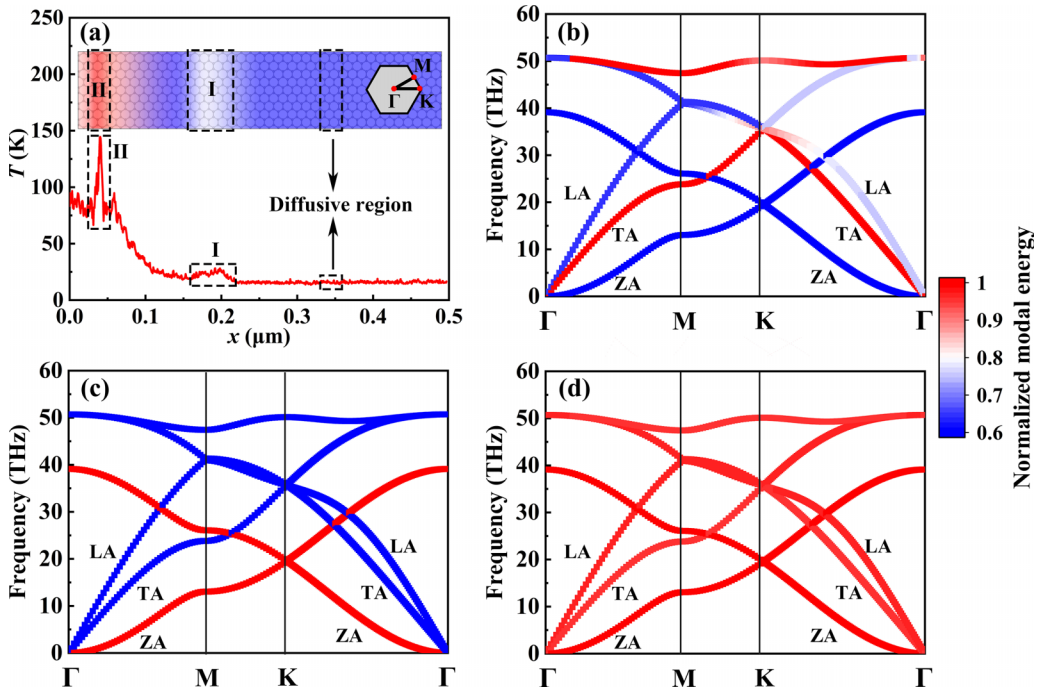

FIG. 2. (a) Schematic figure of the sampling areas (dashed box) for the ballistic pulse, second sound, and diffusive region at 10 ps. Panels (b)–(d) show the normalized modal energy projected into the phonon dispersion of single-layer graphene for (b) ballistic pulse, (c) second sound, and (d) diffusive region. The colors in (b)–(d) represent the magnitude of modal energy.

process, we normalize the phonon modal energy for 350 instantaneous snapshots during 2–26 ps, and then average for each type of regions (two peak regions and a nonpeak region) among different time snapshots to obtain the final phonon modal energy, as shown in Figs. 2(b)–2(d).

Figure 2(b) shows that the averaged modal energy for peak I is dominated by the in-plane mode, i.e., TA and LA modes. Furthermore, the TA phonons have a larger contribution to the ballistic pulse compared to the LA phonons (see, for instance, in the ΓK direction).

Next, we discuss the modal origin for peak II. As shown in Fig. 2(c), the out-of-plane ZA mode makes a dominant contribution to the modal energy compared to the in-plane TA and LA modes, which reveals that the ZA phonon is the origin for peak II. Therefore, the predominance of the ZA phonon demonstrates the second sound nature of this pulse, consistent with the findings from other studies [8,13,15]. Figure 2(c) also shows that the modal energy in each branch is nearly constant for various frequencies and wave vectors, indicating the robustness of phonon hydrodynamics and the dominant role of ZA phonons for second sound over the full Brillion zone. This result demonstrates the fact that the emergence of ZA phonon is a critical signature of hydrodynamic phonon transport as reported in diverse 2D materials [8,13,15], graphite [19], and flexible polymer crystalline [2].

The nonpeak region is investigated from the phonon modal energy analysis in Fig. 2(d). In this region, all phonon modes with different frequencies and wave vectors have a similar contribution to modal energy, indicating the participation of all phonon polarizations in this nonpeak region. As discussed above, the ballistic transport and second sound are contributed by in-plane and out-of-plane phonons, respectively. In contrast, the even contribution among different phonon polarizations reveals the diffusive transport nature in the nonpeak region [31,34].

B. Temperature decay

Different from the diffusive nonpeak region, two peaks of ballistic pulse and second sound propagate with a notable velocity. As gradually dissipating to the environment with ambient temperature T_{amb}, these two peaks are converted to the diffusive transport with a slow propagation velocity. The decay process of second sound should contain many transport physics as previously discussed for the ballistic transport [3,4]. Therefore, we further conduct a parametric study on the decay process of ballistic pulse and second sound in terms of the peak area A and maximum width W, as denoted in the inset of Fig. 3(a). Figure 3(a) shows that the area of second sound peak (A_{sec}) is larger than that of ballistic pulse (A_{bal}), indicating that second sound can carry a larger amount of heat energy than ballistic component during thermal transport. Such phenomenon has also been found in the single-wall carbon nanotube [31], where the energy carried by second sound is much larger than that of the ballistic twisted mode and longitudinal acoustic mode.

Figure 3(a) further depicts that the ballistic pulse decays to zero at 26 ps, while the second sound is preserved for a long time with a slower decay rate. Compared to the fast dissipation of ballistic pulse, the long duration of second sound indicates its low dissipation rate. The maximum width of the peak is also investigated as another signature of dissipation rate for different transport behaviors. Figure 3(b) displays that the maximum width of ballistic pulse (circles) increases

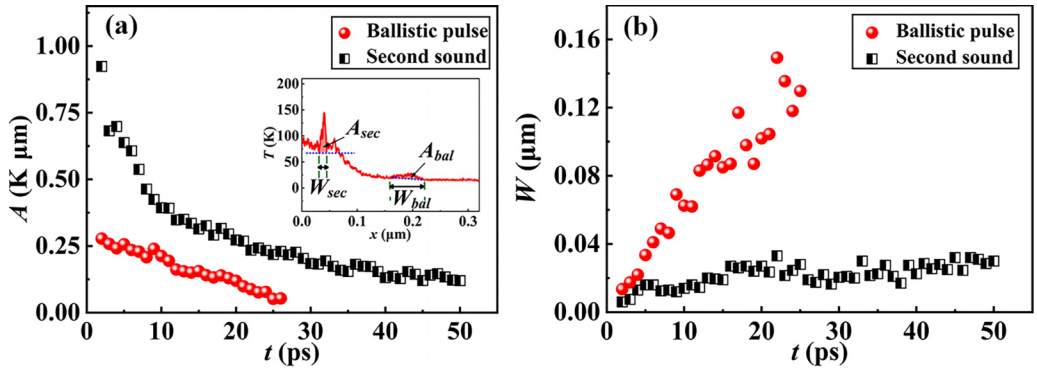

FIG. 3. (a) The area of peaks for ballistic pulse and second sound versus time. The inset labels the definition of peak parameters at $t = 10$ ps. (b) The maximum width of peaks for ballistic pulse and second sound versus time.

much faster with time than that of second sound (squares), indicating a longer lifetime of second sound.

Obviously, the low dissipation rate of second sound would promote the heat transport in the hydrodynamic regime. In addition, it can also support the concept that the predominant momentum-conserving N scattering does not dissipate heat resistively, but can cause the phonon hydrodynamics which can propagate heat more effectively. This feature suggests that the second sound, which carries a large amount of heat, stabilizes for a long time and dissipates at a low rate, holds great potential for the heat dissipation and management applications in the hydrodynamic phonon transport regime.

C. Thickness dependence

The above studies have shown the importance of ZA phonons to second sound and thermal transport in the single-layer graphene. Meanwhile, previous studies [57,58] reported that with increasing number of graphene layers (N), thermal conductivity decreases, due to the fact that the interlayer interactions suppress the contribution from ZA phonons [57]. A recent experiment [30] also revealed that the thickness dependent thermal conductivity is associated with the variation of hydrodynamic phonon transport. To explore the thickness dependent phonon hydrodynamics, we further investigate the propagation of second sound and its phonon modal analysis in the multilayer graphene ($N > 1$) and graphite.

As shown in Fig. 4(a), the peak of second sound still preserves in the multilayer graphene and graphite, which is also dominated by ZA phonons in multilayer graphene [Figs. 4(c) and 4(d)]. Although the height of second sound peak in graphite becomes tiny [see the inset of Fig. 4(a)], the actual

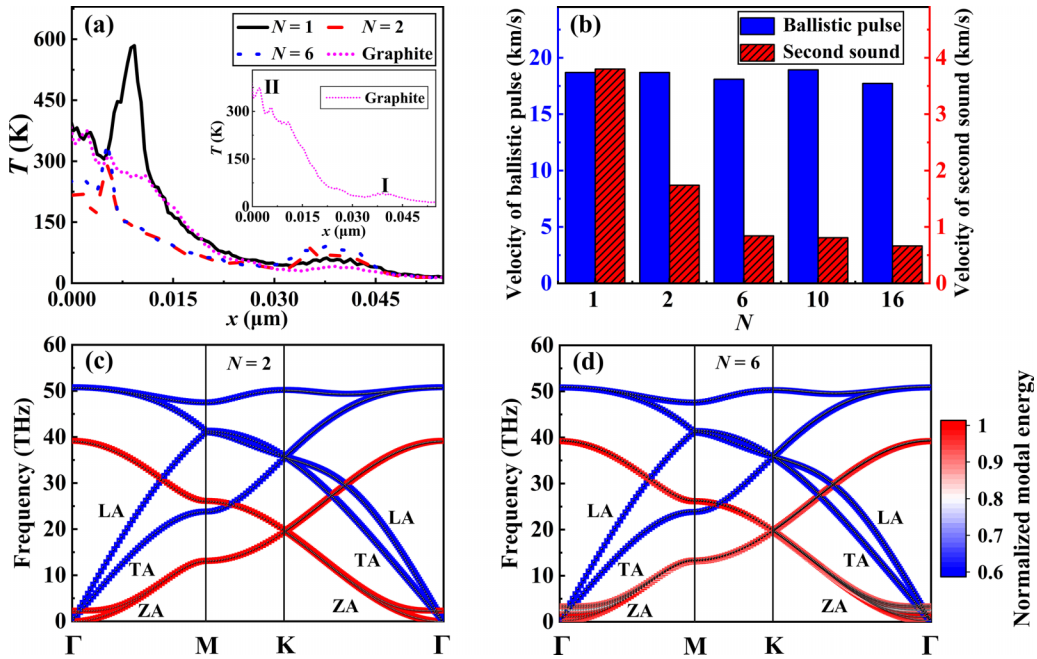

FIG. 4. (a) Thickness dependent transient heat conduction simulation in single-layer graphene ($N = 1$), multilayer graphene (N=2, 6), and graphite at 2 ps. The inset in (a) zooms in for the case of graphite. (b) Velocities of ballistic pulse and second sound versus the layer number. Panels (c) and (d) show the normalized modal energy of second sound projected into the phonon dispersion of multilayer graphene for (c) N=2 and (d) N=6. The colors in (c) and (d) represent the magnitude of normalized modal energy.

contribution of second sound to thermal transport might not be negligible. The recent experiments [10,19] reported that the temperature window of second sound in graphite can reach up to 100 or even 200 K. Furthermore, the propagation velocities of second sound and ballistic pulse are compared in Fig. 4(b). When the thickness increases, the velocity of the ballistic pulse (solid pillar) is almost constant, while the velocity of the second sound (dashed pillar) is suppressed notably. The lower speed of second sound would lead to the faster dissipation of hydrodynamic phonons to the environment, which further causes the suppressed second sound and consequently a reduced thermal conductivity with increasing thickness.

One remarkable feature exhibited in Fig. 4(b) is that when the layer number changes from $N = 1$ to 2, the impact on the velocity of second sound is more significant compared to the case for multilayer graphene ($N > 2$). A similar feature is also observed in Fig. 4(a) that the energy carried by the peak of second sound, i.e., height of the peak, is reduced more substantially for the transition from $N = 1$ to 2, compared to the multilayer case ($N > 2$).

Different from the peak of second sound, the ballistic pulse shows a negligible thickness dependence [see Fig. 4(a) and solid pillar in Fig. 4(b)]. As we discussed before, the ballistic transport is dominated by the in-plane TA and LA modes. The layer stacking along out-of-plane direction has limited impact on the in-plane modes due to the weak interlayer van der Waals interaction, leading to the thickness independent propagation speed of the ballistic pulse.

To explore the origin for the observed layer dependence behavior of second sound, we compare the mode level phonon scattering rate with the same force field used in MD simulation. Here, we generate the force constants in GULP [51] and then calculate three-phonon scattering rates with the SHENGBTE package [59] for both the momentum-conserving N scattering and the momentum nonconserving U scattering, in which the Bose-Einstein distribution is used in the calculation.

The computed phonon scattering rates Γ_N and Γ_U at the ambient temperature of 20 K for $N = 1$, 2, 6 are shown in Figs. 5(a) and 5(b), respectively. When the layer number increases from $N = 1$ to 2, the introduction of interlayer interaction leads to the enhancement of both Γ_N and Γ_U, and such enhancement is particularly strong for the ZA phonon [empty symbols in Figs. 5(a) and 5(b)]. This is because those phonon-phonon scatterings involving an odd number of ZA modes are forbidden in single-layer graphene due to the selection rule induced by the mirror reflection symmetry [38,39], which has also been found to play an important factor in determining thermal transport in other 2D materials [60,61]. As N turns to 2, such selection rule is broken due to the *AB* stacking in bilayer graphene, which can significantly increase the scattering rate for the ZA phonon [see Figs. 5(a) and 5(b)]. The low-frequency optical modes [see Fig. 4(c)] induced by the interlayer interactions can also enhance the U scatterings [30,62,63]. Moreover, compared to the quadratic dispersion of ZA phonon in single-layer graphene, previous studies [64,65] found that the linearization of the ZA branch at very small wave vector **k** would also enhance the weight of U scattering. This point is also witnessed in Fig. 5(b) that Γ_U for the zone-center ZA phonon is substantially enhanced by

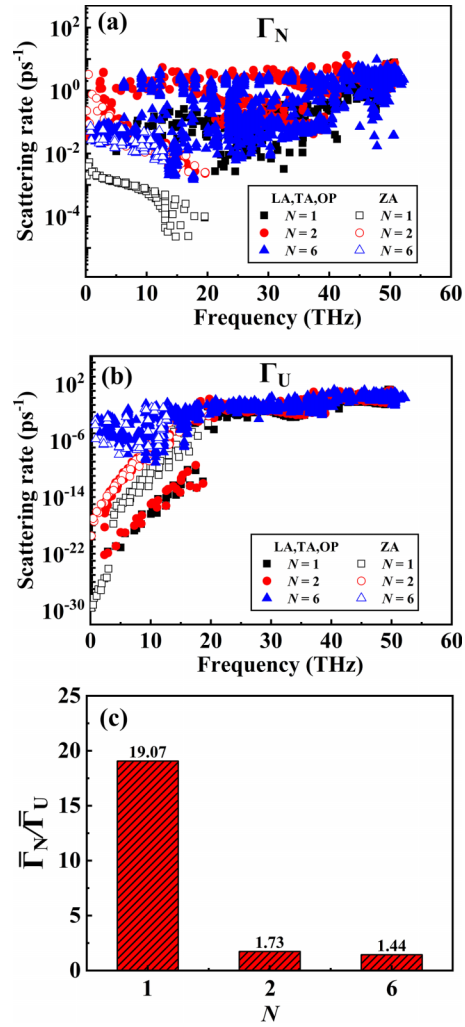

FIG. 5. The frequency-resolved scattering rates for (a) normal scattering Γ_N and (b) umklapp scattering Γ_U at the ambient temperature $T_{amb} = 20$ K in single-layer graphene ($N = 1$) and multilayer graphene (N=2, 6). (c) The ratio between the ensemble-averaged normal scattering rate $\bar{\Gamma}_N$ and umklapp scattering rate $\bar{\Gamma}_U$ for different layer numbers.

more than ten orders of magnitude in our calculations when N increases from 1 to 2, and the enhancement ratio of Γ_U is much larger than that of Γ_N [Fig. 5(a)]. When N further increases from 2 to 6, enhancement of the scattering rate is also observed, particularly for U scattering. These results suggest that although the introduction of interlayer interaction results in the enhancement of both Γ_N and Γ_U, the impact on U scattering is more significant than that on N scattering.

As discussed in Sec. III A, ignoring the quantum effect can affect the absolute value of the second sound velocity, especially at low temperature. In order to more accurately explain the underlying mechanism on the impact of layer number at low temperature, we use quantum statistics to compute the ensemble-averaged scattering rate as [9,66]

$$\bar{\Gamma}_i = \frac{\sum C_k^Q \cdot \Gamma_{k,i}}{\sum C_k^Q}, \tag{5}$$

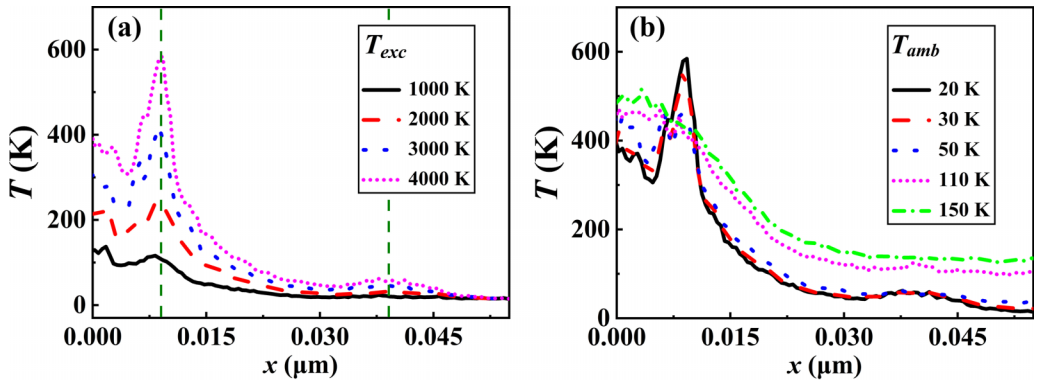

FIG. 6. (a) Transient heat conduction simulation at 2 ps in single-layer graphene with varying T_{exc}. Here T_{amb} is fixed at 20 K. The vertical dashed lines are used to label the position of the ballistic pulse and second sound. (b) Transient heat conduction simulation at 2 ps in single-layer graphene with varying T_{amb}. Here T_{exc} is fixed at 4000 K.

where C_k^Q is the quantum specific heat given by $C_k^Q = n_0[n_0+1]\,(\hbar\omega_k)^2/(k_B T^2)$, and the summation includes all phonon modes. Here n_0 denotes the equilibrium Bose-Einstein distribution function, and i represents N scattering or U scattering.

Figure 5(c) shows the ratio of $\bar{\Gamma}_{\text{N}}/\bar{\Gamma}_{\text{U}}$ which evaluates the relative importance of N scattering over U scattering. In the single-layer graphene, this ratio is 19.07, which suggests the predominance of N scattering. If we only consider those three-phonon processes involving ZA phonons and repeat the calculation, the ratio of $\bar{\Gamma}_{\text{N}}^{\text{ZA}}/\bar{\Gamma}_{\text{U}}^{\text{ZA}}$ can reach 1210.13, highlighting the importance of ZA phonons in the hydrodynamic phonon transport. This result is also consistent with the modal energy analysis in Fig. 2(c), which reveals that peak II is mainly contributed by ZA phonons. As the strong N scattering involving ZA modes is demonstrated as the origin of the second sound and phonon hydrodynamics, peak II should be dominated by the second sound. In the case of bilayer graphene, the ratio of $\bar{\Gamma}_{\text{N}}/\bar{\Gamma}_{\text{U}}$ drops to 1.73, and the ratio of $\bar{\Gamma}_{\text{N}}^{\text{ZA}}/\bar{\Gamma}_{\text{U}}^{\text{ZA}}$ also drops to 4.50, suggesting that the phonon hydrodynamics is weakened in bilayer graphene. As a result, both the peak [Fig. 4(a)] and the velocity [Fig. 4(b)] of second sound are obviously suppressed in bilayer graphene, compared to single-layer graphene. As shown in Fig. 5(c), further increasing layer number to $N = 6$ leads to a minor decrease in the ratio of $\bar{\Gamma}_{\text{N}}/\bar{\Gamma}_{\text{U}}$, which is also consistent with the smaller variation of second sound velocity shown in Fig. 4(b). Therefore, the increased weight of U scattering in multilayer graphene is responsible for the observed layer-dependent behavior of second sound.

D. Temperature effect

To further explore the temperature effect on the fundamental characteristics of second sound in graphene, we finally simulate the transient heat conduction process in single-layer graphene at various thermal excitation temperature T_{exc} and ambient temperature T_{amb}. Figure 6(a) shows although a higher T_{exc} can increase the peak amplitudes of the ballistic pulse and second sound, the positions of the ballistic pulse and second sound (vertical dashed lines) are independent on T_{exc}. In other words, the propagation velocities of the ballistic pulse and second sound are not affected by the thermal excitation temperature T_{exc} in classical MD simulations.

The effect of T_{amb} is displayed in Fig. 6(b). At 110 K, a peak for second sound is still preserved, while it vanishes as T_{amb} increases to 150 K. The increase of T_{amb} completely destroys the peak of second sound after T_{amb} is higher than 110 K, manifesting the significant enhancement of U scattering with the increased T_{amb}. As the N scattering is no longer dominated after 110 K, the second sound phenomenon vanishes. This narrow temperature window for the observation of second sound agrees well with previous reports from experiments and other approaches [2,8,10,12].

It should be pointed out that the temperature-independent second sound velocity observed in Fig. 6 is because of the classical statistics inherently used in MD simulations, in which all phonon modes are equally excited. Under the quantum statistics, the propagation speed of second sound should depend on the ambient temperature T_{amb}, as ZA phonons have a quadratic dispersion and are gradually excited when T_{amb} rises. To illustrate this point, we compute the temperature dependence of the second sound velocity based on Eq. (4) with quantum specific heat given by $C_k^Q = n_0[n_0+1]\,(\hbar\omega_k)^2/(k_B T^2)$. The computed second sound velocity increases with increasing temperature under quantum statistics, while it is temperature independent under classical statistics. The difference between the classical and quantum statistics decreases with increasing temperature (see Fig. S2 of the Supplemental Material [47]).

IV. CONCLUSION

In summary, we have studied the fundamental characteristics of second sound in single-layer and multilayer graphene by a transient heat conduction modeling. The propagations of second sound, ballistic pulse, and diffusive phonons are well demonstrated via the modal energy analysis and propagation speed. Our simulation results show that the ballistic pulse is dominated by the in-plane LA and TA phonons; second sound is contributed by the out-of-plane ZA phonons. In contrast, all phonon polarizations are involved in the diffusive transport. Compared to the ballistic pulse, second sound can carry more heat energy, maintain for a long time, and dissipate at a low rate. In addition, the thickness of multilayer graphene has a significant impact on second sound, due to the enhanced weight of umklapp scattering. A narrow temperature window

for the observation of second sound with upper limit up to 110 K is also found due to the enhanced umklapp scattering at high temperatures. This work provides fundamental characterizations of second sound and modal analysis in single-layer graphene, multilayer graphene, and graphite, which offers important insight into the understanding of the non-Fourier heat conduction and phonon physics in solids.

ACKNOWLEDGMENTS

This project was supported in part by grants from the National Natural Science Foundation of China (Grants No. 12075168 and No. 12205220), and the Science and Technology Commission of Shanghai Municipality (Grant No. 21JC1405600). Z.W.Z. was sponsored by Shanghai Pujiang Program (Grant No. 22PJ1413700).

[1] Y. Guo and M. Wang, Phonon hydrodynamics and its applications in nanoscale heat transport, Phys. Rep. **595**, 1 (2015).

[2] Z. Zhang, Y. Ouyang, Y. Guo, T. Nakayama, M. Nomura, S. Volz, and J. Chen, Hydrodynamic phonon transport in bulk crystalline polymers, Phys. Rev. B **102**, 195302 (2020).

[3] C. Yu, Y. Ouyang, and J. Chen, A perspective on the hydrodynamic phonon transport in two-dimensional materials, J. Appl. Phys. **130**, 010902 (2021).

[4] Z. Zhang, Y. Ouyang, Y. Cheng, J. Chen, N. Li, and G. Zhang, Size-dependent phononic thermal transport in low-dimensional nanomaterials, Phys. Rep. **860**, 1 (2020).

[5] J. Chen, X. Xu, J. Zhou, and B. Li, Interfacial thermal resistance: Past, present, and future, Rev. Mod. Phys. **94**, 025002 (2022).

[6] J. Chen, J. He, D. Pan, X. Wang, N. Yang, J. Zhu, S. A. Yang, and G. Zhang, Emerging theory and phenomena in thermal conduction: A selective review, Sci. China: Phys., Mech. Astron. **65**, 117002 (2022).

[7] X.-P. Luo, Y.-Y. Guo, M.-R. Wang, and H.-L. Yi, Direct simulation of second sound in graphene by solving the phonon Boltzmann equation via a multiscale scheme, Phys. Rev. B **100**, 155401 (2019).

[8] S. Lee, D. Broido, K. Esfarjani, and G. Chen, Hydrodynamic phonon transport in suspended graphene, Nat. Commun. **6**, 6290 (2015).

[9] A. Cepellotti, G. Fugallo, L. Paulatto, M. Lazzeri, F. Mauri, and N. Marzari, Phonon hydrodynamics in two-dimensional materials, Nat. Commun. **6**, 6400 (2015).

[10] S. Huberman, R. A. Duncan, K. Chen, B. Song, V. Chiloyan, Z. Ding, A. A. Maznev, G. Chen, and K. A. Nelson, Observation of second sound in graphite at temperatures above 100 K, Science **364**, 375 (2019).

[11] R. Guyer and J. Krumhansl, Thermal conductivity, second sound, and phonon hydrodynamic phenomena in nonmetallic crystals, Phys. Rev. **148**, 778 (1966).

[12] D. D. Joseph and L. Preziosi, Heat waves, Rev. Mod. Phys. **61**, 41 (1989).

[13] M.-Y. Shang, C. Zhang, Z. Guo, and J.-T. Lü, Heat vortex in hydrodynamic phonon transport of two-dimensional materials, Sci. Rep. **10**, 8272 (2020).

[14] K. Michel, P. Scuracchio, and F. Peeters, Sound waves and flexural mode dynamics in two-dimensional crystals, Phys. Rev. B **96**, 094302 (2017).

[15] P. Scuracchio, K. Michel, and F. Peeters, Phonon hydrodynamics, thermal conductivity, and second sound in two-dimensional crystals, Phys. Rev. B **99**, 144303 (2019).

[16] J. Sussmann and A. Thellung, Thermal conductivity of perfect dielectric crystals in the absence of umklapp processes, Proc. Phys. Soc. **81**, 1122 (1963).

[17] Z. Ding, J. Zhou, B. Song, V. Chiloyan, M. Li, T.-H. Liu, and G. Chen, Phonon hydrodynamic heat conduction and Knudsen minimum in graphite, Nano Lett. **18**, 638 (2018).

[18] R. Whitworth and D. Shoenberg, Experiments on the flow of heat in liquid helium below 0.7 K, Proc. R. Soc. London, Ser. A **246**, 390 (1958).

[19] Z. Ding, K. Chen, B. Song, J. Shin, A. A. Maznev, K. A. Nelson, and G. Chen, Observation of second sound in graphite over 200 K, Nat. Commun. **13**, 285 (2022).

[20] J. Ward and J. Wilks, The velocity of second sound in liquid helium near the absolute zero, London, Edinburgh Dublin Philos. Mag. J. Sci. **42**, 314 (1951).

[21] V. Martelli, J. L. Jiménez, M. Continentino, E. Baggio-Saitovitch, and K. Behnia, Thermal Transport and Phonon Hydrodynamics in Strontium Titanate, Phys. Rev. Lett. **120**, 125901 (2018).

[22] M. Markov, J. Sjakste, G. Barbarino, G. Fugallo, L. Paulatto, M. Lazzeri, F. Mauri, and N. Vast, Hydrodynamic Heat Transport Regime in Bismuth: A Theoretical Viewpoint, Phys. Rev. Lett. **120**, 075901 (2018).

[23] C. C. Ackerman, B. Bertman, H. A. Fairbank, and R. Guyer, Second Sound in Solid Helium, Phys. Rev. Lett. **16**, 789 (1966).

[24] V. Narayanamurti and R. Dynes, Observation of Second Sound in Bismuth, Phys. Rev. Lett. **28**, 1461 (1972).

[25] D. W. Pohl and V. Irniger, Observation of Second Sound in Naf by Means of Light Scattering, Phys. Rev. Lett. **36**, 480 (1976).

[26] H. E. Jackson, C. T. Walker, and T. F. McNelly, Second Sound in NaF, Phys. Rev. Lett. **25**, 26 (1970).

[27] X. Huang, Y. Guo, S. Volz, and M. Nomura, Mapping phonon hydrodynamic strength in micrometer-scale graphite structures, Appl. Phys. Express **15**, 105001 (2022).

[28] Y. Guo, Z. Zhang, M. Bescond, S. Xiong, M. Wang, M. Nomura, and S. Volz, Size effect on phonon hydrodynamics in graphite microstructures and nanostructures, Phys. Rev. B **104**, 075450 (2021).

[29] Y. Guo and M. Wang, Heat transport in two-dimensional materials by directly solving the phonon Boltzmann equation under Callaway's dual relaxation model, Phys. Rev. B **96**, 134312 (2017).

[30] Y. Machida, N. Matsumoto, T. Isono, and K. Behnia, Phonon hydrodynamics and ultrahigh–room-temperature thermal conductivity in thin graphite, Science **367**, 309 (2020).

[31] M. A. Osman and D. Srivastava, Molecular dynamics simulation of heat pulse propagation in single-wall carbon nanotubes, Phys. Rev. B **72**, 125413 (2005).

[32] J. Shiomi and S. Maruyama, Non-Fourier heat conduction in a single-walled carbon nanotube: Classical molecular dynamics simulations, Phys. Rev. B **73**, 205420 (2006).

[33] L. Chen and S. Kumar, Thermal transport in double-wall carbon nanotubes using heat pulse, J. Appl. Phys. **110**, 074305 (2011).
[34] W.-J. Yao and B.-Y. Cao, Thermal wave propagation in graphene studied by molecular dynamics simulations, Chin. Sci. Bull. **59**, 3495 (2014).
[35] K. Ghosh, A. Kusiak, and J.-L. Battaglia, Phonon hydrodynamics in crystalline materials, J. Phys.: Condens. Matter **34**, 323001 (2022).
[36] S. Plimpton, Fast parallel algorithms for short-range molecular dynamics, J. Comput. Phys. **117**, 1 (1995).
[37] A. A. Balandin, Thermal properties of graphene and nanostructured carbon materials, Nat. Mater. **10**, 569 (2011).
[38] L. Lindsay, D. A. Broido, and N. Mingo, Flexural phonons and thermal transport in graphene, Phys. Rev. B **82**, 115427 (2010).
[39] T. Feng and X. Ruan, Four-phonon scattering reduces intrinsic thermal conductivity of graphene and the contributions from flexural phonons, Phys. Rev. B **97**, 045202 (2018).
[40] L. Lindsay and D. Broido, Optimized Tersoff and Brenner empirical potential parameters for lattice dynamics and phonon thermal transport in carbon nanotubes and graphene, Phys. Rev. B **81**, 205441 (2010).
[41] L. A. Girifalco, M. Hodak, and R. S. Lee, Carbon nanotubes, buckyballs, ropes, and a universal graphitic potential, Phys. Rev. B **62**, 13104 (2000).
[42] S. Chen, Q. Wu, C. Mishra, J. Kang, H. Zhang, K. Cho, W. Cai, A. A. Balandin, and R. S. Ruoff, Thermal conductivity of isotopically modified graphene, Nat. Mater. **11**, 203 (2012).
[43] J. Chen, J. H. Walther, and P. Koumoutsakos, Strain engineering of Kapitza resistance in few-layer graphene, Nano Lett. **14**, 819 (2014).
[44] D. Alexeev, J. Chen, J. H. Walther, K. P. Giapis, P. Angelikopoulos, and P. Koumoutsakos, Kapitza resistance between few-layer graphene and water: Liquid layering effects, Nano Lett. **15**, 5744 (2015).
[45] P. Jiang, N. Li, and J. Chen, Observation of kinked soliton structure in realistic materials through wave packet simulations, Phys. Lett. A **451**, 128409 (2022).
[46] W. Götze and K. Michel, First and second sound in crystals, Phys. Rev. **156**, 963 (1967).
[47] See Supplemental Material at http://link.aps.org/supplemental/10.1103/PhysRevB.107.165424 for (1) the verification of different system lengths, and (2) the comparison of second sound velocity calculated with classical and quantum statistics.
[48] P. Jund and R. Jullien, Molecular-dynamics calculation of the thermal conductivity of vitreous silica, Phys. Rev. B **59**, 13707 (1999).
[49] T. Ikeshoji and B. Hafskjold, Non-equilibrium molecular dynamics calculation of heat conduction in liquid and through liquid-gas interface, Mol. Phys. **81**, 251 (1994).
[50] T. Feng, W. Yao, Z. Wang, J. Shi, C. Li, B. Cao, and X. Ruan, Spectral analysis of nonequilibrium molecular dynamics: Spectral phonon temperature and local nonequilibrium in thin films and across interfaces, Phys. Rev. B **95**, 195202 (2017).
[51] J. D. Gale, GULP: A computer program for the symmetry-adapted simulation of solids, J. Chem. Soc., Faraday Trans. **93**, 629 (1997).
[52] Y. Ouyang, C. Yu, J. He, P. Jiang, W. Ren, and J. Chen, Accurate description of high-order phonon anharmonicity and lattice thermal conductivity from molecular dynamics simulations with machine learning potential, Phys. Rev. B **105**, 115202 (2022).
[53] S. Hu, J. Chen, N. Yang, and B. Li, Thermal transport in graphene with defect and doping: Phonon modes analysis, Carbon **116**, 139 (2017).
[54] Z. Zhang, S. Hu, J. Chen, and B. Li, Hexagonal boron nitride: A promising substrate for graphene with high heat dissipation, Nanotechnology **28**, 225704 (2017).
[55] Z. Ding, J. Zhou, B. Song, M. Li, T.-H. Liu, and G. Chen, Umklapp scattering is not necessarily resistive, Phys. Rev. B **98**, 180302(R) (2018).
[56] X. Gu, Z. Fan, and H. Bao, Thermal conductivity prediction by atomistic simulation methods: Recent advances and detailed comparison, J. Appl. Phys. **130**, 210902 (2021).
[57] J. H. Seol *et al.*, Two-dimensional phonon transport in supported graphene, Science **328**, 213 (2010).
[58] S. Ghosh, W. Bao, D. L. Nika, S. Subrina, E. P. Pokatilov, C. N. Lau, and A. A. Balandin, Dimensional crossover of thermal transport in few-layer graphene, Nat. Mater. **9**, 555 (2010).
[59] W. Li, J. Carrete, N. A. Katcho, and N. Mingo, ShengBTE: A solver of the Boltzmann transport equation for phonons, Comput. Phys. Commun. **185**, 1747 (2014).
[60] S. Lu, W. Ren, J. He, C. Yu, P. Jiang, and J. Chen, Enhancement of the lattice thermal conductivity of two-dimensional functionalized MXenes by inversion symmetry breaking, Phys. Rev. B **105**, 165301 (2022).
[61] C. Yu, Y. Hu, J. He, S. Lu, D. Li, and J. Chen, Strong four-phonon scattering in monolayer and hydrogenated bilayer BAs with horizontal mirror symmetry, Appl. Phys. Lett. **120**, 132201 (2022).
[62] H. Song, J. Liu, B. Liu, J. Wu, H.-M. Cheng, and F. Kang, Two-dimensional materials for thermal management applications, Joule **2**, 442 (2018).
[63] D. Nika, E. Pokatilov, A. Askerov, and A. Balandin, Phonon thermal conduction in graphene: Role of Umklapp and edge roughness scattering, Phys. Rev. B **79**, 155413 (2009).
[64] L. Lindsay, D. Broido, and N. Mingo, Flexural phonons and thermal transport in multilayer graphene and graphite, Phys. Rev. B **83**, 235428 (2011).
[65] L. Paulatto, F. Mauri, and M. Lazzeri, Anharmonic properties from a generalized third-order *ab initio* approach: Theory and applications to graphite and graphene, Phys. Rev. B **87**, 214303 (2013).
[66] J. Jiang, S. Lu, Y. Ouyang, and J. Chen, How hydrodynamic phonon transport determines the convergence of thermal conductivity in two-dimensional materials, Nanomaterials **12**, 2854 (2022).